Published in final edited form as:
Nat Nanotechnol. 2012 October ; 7(10): 677–682. doi:10.1038/nnano.2012.146.

M13-templated magnetic nanoparticles for targeted in vivo imaging of prostate cancer

Debadyuti Ghosh[1,2], **Youjin Lee**[1], **Stephanie Thomas**[3], **Aditya G. Kohli**[1], **Dong Soo Yun**[1], **Angela M. Belcher**[1,2,4,*], and **Kimberly A. Kelly**[3,*]

[1]Department of Materials Science and Engineering, Massachusetts Institute of Technology, Cambridge, Massachusetts 02139, USA

[2]Koch Institute for Integrative Cancer Research, Massachusetts Institute of Technology, Cambridge, Massachusetts 02139, USA

[3]Biomedical Engineering and Robert M. Berne Cardiovascular Research Center, University of Virginia, Charlottesville, Virginia 22904, USA

[4]Department of Biological Engineering, Massachusetts Institute of Technology, Cambridge, Massachusetts 02139, USA

Abstract

Molecular imaging allows clinicians to visualize the progression of tumours and obtain relevant information for patient diagnosis and treatment[1]. Owing to their intrinsic optical, electrical and magnetic properties, nanoparticles are promising contrast agents for imaging dynamic molecular and cellular processes such as protein-protein interactions, enzyme activity or gene expression[2]. Until now, nanoparticles have been engineered with targeting ligands such as antibodies and peptides to improve tumour specificity and uptake. However, excessive loading of ligands can reduce the targeting capabilities of the ligand[3,4,5] and reduce the ability of the nanoparticle to bind to a finite number of receptors on cells[6]. Increasing the number of nanoparticles delivered to cells by each targeting molecule would lead to higher signal-to-noise ratios and improve image contrast. Here, we show that M13 filamentous bacteriophage can be used as a scaffold to display targeting ligands and multiple nanoparticles for magnetic resonance imaging of cancer cells and tumours in mice. Monodisperse iron oxide magnetic nanoparticles assemble along the M13 coat, and its distal end is engineered to display a peptide that targets SPARC glycoprotein, which is overexpressed in various cancers. Compared with nanoparticles that are directly functionalized with targeting peptides, our approach improves contrast because each SPARC-targeting molecule

[*]Authors for correspondence: Kimberly A. Kelly Department of Biomedical Engineering and the Robert M. Berne Cardiovascular Research Center University of Virginia PO Box 800759 Charlottesville VA, 22904 Kak3x@virginia.edu; Angela M. Belcher Departments of Materials Science and Engineering and Biological Engineering Koch Institute for Integrative Cancer Research Massachusetts Institute of Technology 77 Massachusetts Ave., 76-561 Cambridge, MA 02139 belcher@mit.edu.

Author Contributions D.G., K.A.K, and A.M.B. conceived and designed the experiments. D.G., Y.L., and S.T. performed experiments. D.G., Y.L., S.T., and A.G.K. contributed new reagents. D.S.Y. conducted high-resolution transmission electron microscopy. D.G. and K.A.K. analysed data. D.G., K.A.K., and A.M.B. co-wrote the paper.

Additional Information Supplementary information is available in the online version of the paper.

Competing Financial Interests The authors declare no competing financial interests.

delivers a large number of nanoparticles into the cells. Moreover, the targeting ligand and nanoparticles could be easily exchanged for others, making this platform attractive for in vivo high-throughput screening and molecular detection.

M13 is a filamentous virus with five genetically modifiable coat proteins (p3, p6, p7, p8, and p9) for peptide or protein display. Previously, phage display has been exploited for epitope discovery[7], gene delivery[8], antibody delivery[9], and *in vitro* and *in vivo* ligand discovery[10,11]. Although phage display allows rapid, amplifiable screening of lead molecules for targeting, the genetic and physical properties of M13 also make it an excellent biological building block for bottom-up fabrication and assembly of materials[12]. The highly ordered structure of the 2700 copies of the major coat protein p8 and the filamentous shape of M13 (~6.5 nm in diameter and ~880 nm in length) allows the phage to multivalently interact with nanomaterials. Our lab has engineered M13 for display of material-specific peptides on p3 and p8 as a template to grow and nucleate various inorganic materials for applications including high power Li ion batteries and photocatalytic water splitting[13,14]. Here, we extend this work and report the development of M13 bacteriophage as a vector incorporating a tumour-targeting peptide[15] and a peptide motif for templated assembly of magnetic iron oxide nanoparticles (MNPs) towards nanoparticle-mediated, dark contrast-based magnetic resonance imaging for specific tumour detection (Fig. 1a). We investigate selective tumour targeting against prostate cancer xenograft models expressing different levels of secreted protein, acidic and rich in cysteine (SPARC), which is upregulated in various cancers (reviewed in [16]) and correlated with poor prognosis[16]. The capsid organization of M13 spatially separates targeting and imaging moieties, circumventing any potential problems with ligand or probe functionality. Using p3 to display targeting ligands while assembling multiple MNPs along the p8 capsid (Fig.1a) achieves targeting and delivers a larger payload of MNPs per SPARC compared with directly functionalized nanoparticles.

Previously, we engineered multiple glutamic acid residues on the N-terminus of the major coat capsid protein p8 on M13 for assembly of various metal oxides for anode battery and layer-by-layer polymer assembly applications[17]. At physiological pH, the triglutamate peptide-modified M13 has a net negative charge, allowing for electrostatic assembly with positively charged moieties, such as positively charged nanoparticles[17]. Further, to create a molecularly targeted M13, a SPARC-binding peptide (SPPTGIN, designated as SBP) identified using phage display[15] was genetically engineered into the p3 minor coat protein of triglutamate modified M13 (Fig. 1a); in the presence of MNPs, the resulting phage is designated as M13-SBP-MNP.

We then synthesized crystalline, monodisperse iron oxide nanoparticles to assemble along the modified M13 (Fig. 2 and Supplementary Note 1). We confirmed the monodispersity by transmission electron microscopy (TEM) and dynamic light scattering (DLS, Fig. 2). From high-resolution TEM, the particles demonstrated distinct lattice fringe patterns, suggesting a highly crystalline structure (Fig. 2, top row, left column, inset). X-ray diffraction confirmed the cubic spinel structure of the iron oxide nanoparticles, whereas a d-spacing comparison corroborated previous reports that iron oxide particles are either maghemite (γ-Fe_2O_3) or

magnetite (Fe_3O_4)[18] (Supplementary Fig. S1 and Table S1). These particles were water-solubilized with a PEG-lipid formulation (Supplementary Note 1) and were stable in water for at least two months (Supplementary Fig. S2).

We characterized the assembly of the nanoparticles along the coat of M13. MNPs were mixed with M13-expressing triglutamate motif and allowed to assemble along the length of the virus. TEM confirmed multivalent MNP assembly along the virus (Fig. 2, top row, right column). Previous work has shown M13-templated materials with and without engineered p3 ligands have similar materials properties[13]. MNPs are aligned in a filamentous orientation along the p8 coat with a length of approximately ~ 800 nm, which is the approximate length of M13. The number of MNPs per M13 was quantified by iron content using inductive coupled plasma atomic emission spectroscopy (ICP-AES) (Supplementary Note 2). Using iron standards, we measured the emission intensities and made a calibration curve (Supplementary Fig. S3) to interpolate iron content of M13-templated MNPs from measured intensities and calculate the number of MNPs per virus. There are approximately 26 particles per M13, confirming multivalent assembly as observed by TEM. From dynamic light scattering, M13 and M13-assembled MNPs are monodisperse, with a radius of ~147.3 nm (Supplementary Fig. S4) and ~181.4 nm (Fig. 2, bottom row, right column), respectively. Importantly, M13-assembled MNPs have a single histogram population and lack multiple peaks, suggesting the nanoparticles stably complex with the virus and do not aggregate into multiple populations. The increase in size of M13-MNP compared with M13 can be attributed to multiple MNPs assembling on the 2700 p8 copies. M13-MNP is stable in other biological solutions including PBS (Supplementary Note 3 and Supplementary Fig. S5), culture media and serum for at least three weeks (Fig. 2) and is not cytotoxic by standard WST-1 cell proliferation assay (Supplementary Fig. S6). Virus-nanoparticle complexes are stable and non-toxic in physiological conditions, which makes them attractive for *in vivo* imaging.

To investigate the magnetic resonance (MR) contrast potential of MNPs and M13-MNPs, we measured the transverse relaxation (T2). Proton relaxivity is a rate of proton relaxation in response to iron atom concentration. Paramagnetic iron oxide nanoparticles cause local inhomogenities in the magnetic field resulting in decoherence of the water proton precession of the spins. The resulting relaxation of the spins until the magnetization decays to zero causes a negative, or ‘dark’ contrast in the background of the light MR image. We measured the T2 of MNPs and M13-MNPs and determined relaxivity based on the iron concentration of the MNPs (Table 1 and Supplementary Fig. S7). MNPs and M13-MNP had comparable relaxivities of 65.1 mM^{-1} s^{-1} and 58.7 mM^{-1} s^{-1}, respectively. Their relaxivities are an improvement over those of several superparamagnetic iron oxide particles including ferumoxtran and monocrystalline iron oxide nanoparticles (Table 1), which exhibit relaxivities of 35.3 and 34.8 mM^{-1} s^{-1}, respectively[19,20]. These clinically used particles possess lower R2 relaxivities compared with our crystalline particles since they are synthesized in aqueous media and thus have poorer crystallinity[21]. Ferumoxides including Feridex (Table 1) demonstrate higher relaxivities (107 mM^{-1} s^{-1}) than synthesized MNPs and M13-MNP, probably a result of their multiple crystalline domains[22]. Nevertheless, the

enhanced contrast properties of M13-MNP compared with several clinically used particles highlight its potential as an *in vivo* imaging probe.

After we validated SPARC-binding peptide is displayed on M13 in the presence of MNPs and targets SPARC-expressing C4-2B prostate cancer cell line (Supplementary Note 4 and Supplementary Figs. S8 and S9), we investigated selectivity of targeting against cell lines expressing different levels of SPARC. DU145 control (low SPARC expressing) and C4-2B (higher level of SPARC expression) cell lines were incubated with M13-SBP-MNP at two different virus concentrations and relaxation times were measured from harvested cell lysates. At both concentrations, there was approximately a threefold decrease in relaxation times of M13-SBP-MNP incubated C4-2B lysates when compared with DU145 cell lysates, suggesting selective and specific uptake of M13-SBP-MNP (Fig. 1b). The increase in targeting can be attributed to differences of cellular SPARC expression levels between C4-2B and DU145 cells. From quantitative flow cytometry (Supplementary Note 5), we determined C4-2B expressed 5870±565 SPARC molecules per cell, whereas DU145 had 3395±633 copies per cell (Supplementary Figs. S10 and S11). This suggests while C4-2B expresses higher levels of SPARC *in vitro* compared with control DU145, there is SPARC expression present in DU145 cells. It is important to note since SPARC is a matricellular stromal protein, there will be differences between expression levels in cell lines and tumours.

We next examined SPARC-targeted imaging of prostate cancer *in vivo*. C4-2B and DU145 cells were injected subcutaneously in immunodeficient mice and, on tumour formation, M13-SBP-MNP was injected intravenously and allowed to circulate for 24 h. Mice with tumours were scanned pre-injection and 24 h post-injection via a 7 T magnetic resonance imaging (MRI) scanner with a T2*-weighted pulse sequence. Importantly, mice with C4-2B-derived tumours demonstrated a decrease in MR signal 24 hours after injection of SPARC-targeted phage (Fig. 3a,b). Mice bearing DU145 tumours had tumours that remained bright after injection of contrast agent (Fig. 3c,d), indicating uptake of M13-SBP-MNP is specific to C4-2B tumours. Pixel intensity due to iron uptake in the tumours was measured to quantify dark contrast signal enhancement (Fig. 3e). Compared with DU145, there is an approximately sixfold decrease in pixel intensity (per cm^2) in C4-2B (Fig. 3e). The intensity decrease implies there is a darkening of the MR signal in C4-2B owing to increased M13-SBP-MNP uptake, compared with DU145 controls. We corroborated the imaging with correlative histology. Tumour sections were stained with haematoxylin and eosin (H&E) and Perl's reagent for the presence of iron from MNPs. As expected from the MRI findings, sections of tumour derived from C4-2B cells stained blue with Perl's reagent (Fig. 3f, top row, middle column), whereas DU145 tumours had little to no staining, indicating a lack of iron present in the tumour (Fig. 3f, bottom row, middle column). Iron staining in the extracellular matrix is present in areas of SPARC expression[23] of C4-2B tumours (Fig. 3f, top row, right column) whereas control DU145 tumours do not stain for SPARC expression, which suggests uptake is specific to SPARC expression.

As previously mentioned, most work focuses upon functionalizing each nanoparticle with multiple ligands to improve binding, but the number of cell surface targets and their accessibility in cell lines and tumours limit targeting efficiency and subsequent delivery of

these agents[6]. One approach to improve targeting of agents such as drugs and nanoparticles is to develop carriers able to deliver multiple agents per receptor[6]. We investigated the ability of M13 to deliver multiple MNPs per SPARC molecule for potential signal amplification (Fig. 4a). C4-2B cells were incubated with either fluorescently tagged M13-SBP-MNP or functionalized MNPs with equivalent amounts of targeting peptide to bind and saturate SPARC, accounting for five peptides on p3 per M13 and four and eight peptides per functionalized nanoparticles at the low and high densities, respectively. After 1 h, there is a threefold increase in fluorescence with M13-SBP-MNP compared with MNPs functionalized with the two different concentrations of SBP (Fig. 4b). The fluorescence of M13-SBP-MNP uptake increases after 4 h, with a 11-fold improvement compared with functionalised MNPs (Fig. 4b). To investigate the potential for enhanced contrast the T2 relaxation of incubated cell lysates was measured. There is a 18-fold decrease in relaxivity per particle in lysates targeted with M13-SBP-MNP compared with low SBP-MNP (Fig. 4c), indicating greater delivery of MNPs using M13 improves the relaxation signal. These results suggest M13 is an effective scaffold for amplified targeting *in vitro* and has the potential to further enhance dark contrast imaging *in vivo*.

We have demonstrated M13 as a nanoscale scaffold that integrates phage-presenting targeting ligands and nanoparticle assembly for molecularly targeted, amplified imaging of prostate cancer. Our virus-nanoparticle complexes are stable and exhibit improved MR contrast potential compared with several clinically used superparamagnetic iron oxide particles. Recent work has reported MNPs with higher relaxivities, obtained by altering the composition through doping[24] or oxidation[25]. These synthesized particles could be multivalently assembled using M13 scaffold for further signal enhancement. Using our system, we demonstrate higher delivery of MNPs per target than traditional nanoparticle approaches, and this novel targeting approach can be coupled with other amplification strategies including bioorthogonal chemistries for pre-targeting[26] or communicating nanoparticle systems[27] to further increase nanoparticle delivery. Interestingly, the low number of SPARC binding peptide per M13 (~1 peptide per 5 nanoparticles) is almost comparable to non-modified MNPs; regardless of this, M13 still achieves improved targeting *in vitro* compared with peptide-functionalized MNPs (Fig. 4) and selective targeting *in vivo* (Fig. 3). This highlights the potential of M13 as a carrier for effective delivery without the need for high presentation of targeting ligands. Although previous reports of *in vivo* phage targeting has focused on the vasculature[11,28] and lymphatic system[29], homing to the tumour stroma suggests the ability of phage to penetrate into the tumour. Future work will involve investigating mechanism of M13 tumour uptake *in vivo*.

As M13 can be easily genetically engineered for peptide display, numerous functionalities can be encoded for incorporating other imaging moieties for multimodal imaging or possibly chemotherapeutic agents for drug delivery and therapy. We have recently shown by re-engineering the p9 coat protein of M13, we can incorporate and spatially control drugs alongside imaging and targeting moieties (unpublished results). The genetic control and modularity of the M13 platform make it a useful and powerful screening tool to identify promising imaging agents for tumour detection and stratification and investigate other diseases such as atherosclerosis[30], beta cells in diabetes, as well as bacterial infections.

Methods

Cell lines and culture

DU145 human prostate cancer cell lines were purchased from American Type Culture Collection (ATCC). C4-2B cells were provided courtesy of Dr. Michael Weber (University of Virginia). DU145 was grown in Dulbecco's Minimum Essential Medium (DMEM) supplemented with 10% FBS (Hyclone) and 1% penicillin/streptomycin (Life Technologies) at 37°C in 5% CO_2. C4-2B were grown in T-medium (Life Technologies) with 10% FBS and pencillin/streptomycin (Life Technologies).

Complexation of M13 with MNPs

Molar excess of water-soluble, aminated iron oxide MNPs (synthesis described in Supplementary Note 1) were mixed with M13 expressing triglutamate motif and optimized to get ~26 nanoparticles per virus. Virus-MNP complexes were precipitated by standard PEG/NaCl precipitation, thereby removing unbound, excess particles present the supernatant. The virus-MNP complexes were resupsended in either water or PBS. The number of MNPs per virus was quantified by measuring iron content using ICP-AES spectroscopy (see Supplementary Note 2), interpolating the amount of iron in the sample against a standard curve and calculating the number of iron oxide particles per virus.

TEM and HRTEM of iron oxide MNPs and M13-templated MNPs

For high-resolution transmission electron microscopy, JEOL 2010F TEM was used. For TEM analysis, MNPs and virus-templated MNPs solutions were dropped on carbon copper holey grid (Ted Pella), washed with ddH_2O several times and dried.

Dynamic light scattering

To determine the size of MNPs and virus-MNP complexes in various aqueous and buffer conditions, samples were measured using a DynaPro Titan Light Scattering Instrument. Samples were loaded in 20 uL cuvettes and run at 10% power (to prevent saturated counts). Measurements were collected at 10 s intervals. Each sample was run 10 times.

Magnetometer measurements

Cells were harvested and lysed with cell lysis buffer (PBS + 0.1% Triton X-100 + 1% SDS). Transverse relaxation times of cell lysates were measured using a Bruker 0.47T minispec q20 (Bruker Optics) at 40°C. Relaxivity was calculated by measuring T2 relaxation times of samples and plotting the inverse relaxation times against the iron concentration of the sample and taking the slope.

Targeting *in vitro*

For experiments involving cell lines, 100,000 cells were seeded in 24-well tissue culture plates (BD Biosciences) in appropriate tissue culture media. Cell lines were incubated with virus-templated, non-functionalized or functionalized MNPs in PBS, depending on the experiment. Samples were incubated at 37°C for 1, 4, or 24 h and then collected in 300 uL

lysis buffer (PBS supplemented with 1% SDS and 0.1% Triton X-100) and incubated on ice for 30 minutes before being measured by table-top relaxometer or flow cytometry.

Flow cytometry

For cell targeting experiments *in vitro*, MNPs, M13-MNP, and M13-SBP-MNP were labelled with either 10 ug mL^{-1} Alexa Fluor 680 or Alexa Fluor 488 succinimidyl ester (Life Technologies). After conjugation, samples were dialyzed to remove unconjugated dye using a dialysis bag with a 12,000-14,000 molecular weight cut-off (Spectrum Labs). Cells incubated with samples were washed and collected using trypsin-EDTA (Life Technologies). Collected cells were neutralized with complete media with 10% FBS and washed twice with 2% FBS in PBS. Cells were run on FACScalibur (Becton Dickinson). Uptake as measured by mean fluorescence was analysed from 10,000 gated events. Samples were run in triplicate.

Targeting *in vivo*

DU145 and C4-2B cells were trypsinized from tissue culture plates and collected. A total of 2×10^6 DU145 and C4-2B cells each were resuspended in PBS. C4-2B cells were resuspended in a 1:1 solution of Matrigel (BD Biosciences) to PBS, and cell lines were injected subcutaneously above both flanks of 7- to 9- week-old athymic nu/nu mice (Charles River) weighing ~30 g, with n = 5 for each cohort. Tumours were grown 3-5 weeks to ~3-5 mm diameter for *in vivo* targeted imaging experiments. Tumoured mice were injected with 1×10^{12} plaque-forming units of M13-SBP-MNP in PBS (with ~20 mg kg^{-1} iron concentration) via tail-vein and imaged 24 h post-injection using a 7T Pharmascan MR small animal scanner (Bruker). Samples were imaged with weighted T2*. Images were obtained with TE = 10 ms. Images were processed and analysed with OsiriX imaging software. To quantify the pixel intensity of mice injected with M13-SBPMNP probe bearing either C4-2B or DU145 tumours, images were collected at the same imaging depth (same z plane or depth) of each mouse and regions of interest (ROI) with equivalent areas (~0.1 cm^2) were drawn around the tumoured areas. The pixel intensity was calculated and normalized to the area from the ROI.

Correlative Histology

After imaging, animals were sacrificed and tumours were excised and frozen in optimal cutting temperature (OCT). Serial frozen sections were stained with H&E or for the presence of iron using Perl's reagent. Sections were stained for SPARC expression using antibody against SPARC (R&D Systems). Images were taken with an Olympus IX51 inverted microscope at various magnifications and processed with camera software.

Supplementary Material

Refer to Web version on PubMed Central for supplementary material.

Acknowledgments

This work was supported by NIH Center for Cancer Nanotechnology Excellence U54-CA151884 and NIH NCI RO1 CA137071. The authors thank Jack Roy with assistance with MRI and Fred Reynolds with excellent technical

assistance. We would also like to thank Melissa Bevard for immunohistochemistry assistance. We would also like to thank Debby Pheasant and the Biophysical Instrumentation Facility for use of the DLS. The authors also thank Dr. Jennifer Hsieh with help with XRD. The authors also thank the Center for Materials Science and Engineering for use of the ICP-AES and TEM. We would also like to acknowledge the Koch Institute Swanson Biotechnology Center for DNA sequencing.

References

1. Weissleder R. Molecular imaging in cancer. Science's STKE. 2006; 312:1168–1171.
2. Massoud T, Gambhir S. Molecular imaging in living subjects: seeing fundamental biological processes in a new light. Genes & development. 2003; 17:545–580. [PubMed: 12629038]
3. Gu F, et al. Precise engineering of targeted nanoparticles by using self-assembled biointegrated block copolymers. Proc Natl Acad Sci U S A. 2008; 105:2586–2591. [PubMed: 18272481]
4. Hamblett KJ, et al. Effects of drug loading on the antitumor activity of a monoclonal antibody drug conjugate. Clinical Cancer Research. 2004; 10:7063–7070. [PubMed: 15501986]
5. Hlavacek W, Posner R, Perelson A. Steric effects on multivalent ligand-receptor binding: exclusion of ligand sites by bound cell surface receptors. Biophysical Journal. 1999; 76:3031–3043. [PubMed: 10354429]
6. Ruoslahti E, Bhatia SN, Sailor MJ. Targeting of drugs and nanoparticles to tumors. Journal of Cell Biology. 2010; 188:759–768. [PubMed: 20231381]
7. Scott JK, Smith GP. Searching for peptide ligands with an epitope library. Science. 1990; 249:386–390. [PubMed: 1696028]
8. Larocca D, Witte A, Johnson W, Pierce GF, Baird A. Targeting bacteriophage to mammalian cell surface receptors for gene delivery. Hum. Gene Ther. 1998; 9:2393–2399. [PubMed: 9829538]
9. Frenkel D, Solomon B. Filamentous phage as vector-mediated antibody delivery to the brain. Proceedings of the National Academy of Sciences of the United States of America. 2002; 99:5675–5679. [PubMed: 11960022]
10. Barry MA, Dower WJ, Johnston SA. Toward cell-targeting gene therapy vectors: selection of cell-binding peptides from random peptide-presenting phage libraries. Nat Med. 1996; 2:299–305. [PubMed: 8612228]
11. Arap W, Pasqualini R, Ruoslahti E. Cancer treatment by targeted drug delivery to tumor vasculature in a mouse model. Science. 1998; 279:377–380. [PubMed: 9430587]
12. Mao CB, et al. Virus-based toolkit for the directed synthesis of magnetic and semiconducting nanowires. Science. 2004; 303:213–217. [PubMed: 14716009]
13. Lee YJ, et al. Fabricating Genetically Engineered High-Power Lithium-Ion Batteries Using Multiple Virus Genes. Science. 2009; 324:1051–1055. [PubMed: 19342549]
14. Nam YS, et al. Biologically templated photocatalytic nanostructures for sustained light-driven water oxidation. Nature Nanotechnology. 2010; 5:340–344.
15. Kelly KA, Waterman P, Weissleder R. In vivo imaging of molecularly targeted phage. Neoplasia. 2006; 8:1011–1018. [PubMed: 17217618]
16. Clark CJ, Sage EH. A prototypic matricellular protein in the tumor microenvironment--where there's SPARC, there's fire. J Cell Biochem. 2008; 104:721–732. [PubMed: 18253934]
17. Yoo PJ, et al. Spontaneous assembly of viruses on multilayered polymer surfaces. Nat Mater. 2006; 5:234–240. [PubMed: 16489350]
18. Park J, et al. Ultra-large-scale syntheses of monodisperse nanocrystals. Nature Materials. 2004; 3:891–895.
19. Shen T, Weissleder R, Papisov M, Bogdanov A Jr. Brady TJ. Monocrystalline iron oxide nanocompounds (MION): physicochemical properties. Magn Reson Med. 1993; 29:599–604. [PubMed: 8505895]
20. Fan X, et al. Differentiation of nonmetastatic and metastatic rodent prostate tumors with high spectral and spatial resolution MRI. Magn Reson Med. 2001; 45:1046–1055. [PubMed: 11378883]
21. Lee N, et al. Magnetosome-like ferrimagnetic iron oxide nanocubes for highly sensitive MRI of single cells and transplanted pancreatic islets. Proc Natl Acad Sci U S A. 2011; 108:2662–2667. [PubMed: 21282616]

22. Jung CW, Jacobs P. Physical and chemical properties of superparamagnetic iron oxide MR contrast agents: ferumoxides, ferumoxtran, ferumoxsil. Magn Reson Imaging. 1995; 13:661–674. [PubMed: 8569441]

23. Brekken R, Sage E. SPARC, a matricellular protein: at the crossroads of cell-matrix. Matrix Biology. 2000; 19:569–580. [PubMed: 11102747]

24. Lee JH, et al. Artificially engineered magnetic nanoparticles for ultra-sensitive molecular imaging. Nat Med. 2007; 13:95–99. [PubMed: 17187073]

25. Yoon TJ, Lee H, Shao H, Weissleder R. Highly magnetic core-shell nanoparticles with a unique magnetization mechanism. Angew Chem Int Ed Engl. 2011; 50:4663–4666. [PubMed: 21495138]

26. Haun JB, Devaraj NK, Hilderbrand SA, Lee H, Weissleder R. Bioorthogonal chemistry amplifies nanoparticle binding and enhances the sensitivity of cell detection. Nat Nanotechnol. 2010; 5:660–665. [PubMed: 20676091]

27. von Maltzahn G, et al. Nanoparticles that communicate in vivo to amplify tumour targeting. Nat Mater. 2011; 10:545–552. [PubMed: 21685903]

28. Pasqualini R, Ruoslahti E. Organ targeting in vivo using phage display peptide libraries. Nature. 1996; 380:364–366. [PubMed: 8598934]

29. Laakkonen P, Porkka K, Hoffman J, Ruoslahti E. A tumor-homing peptide with a targeting specificity related to lymphatic vessels. Nature medicine. 2002; 8:751–755.

30. Kelly K, et al. Detection of vascular adhesion molecule-1 expression using a novel multimodal nanoparticle. Circulation research. 2005; 96:327–336. [PubMed: 15653572]

31. Schellenberger EA, Sosnovik D, Weissleder R, Josephson L. Magneto/optical annexin V, a multimodal protein. Bioconjug Chem. 2004; 15:1062–1067. [PubMed: 15366960]

32. Kellar KE, et al. Important considerations in the design of iron oxide nanoparticles as contrast agents for TI-weighted MRI and MRA. Acad Radiol. 2002; 9(Suppl 1):S34–37. [PubMed: 12019889]

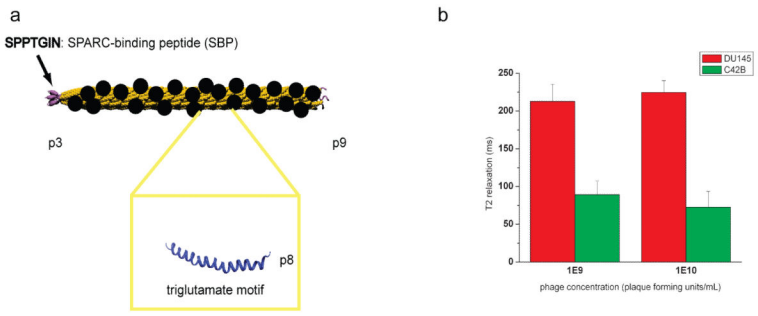

Figure 1. Schematic and targeting *in vitro* of M13-templated magnetic nanoparticles for MR imaging

a, Schematic of M13 (yellow) with SPARC binding peptide displayed on p3 protein of virus (in pink). p8 proteins displaying triglutmate motif for multivalent assembly and display of iron oxide nanocrystals (denoted as black circles) along the viral coat. **b,** Cell-specific targeting of various concentrations of M13-SBP-MNP against DU145 (low SPARC expression) and C4-2B (SPARC expressing) cell lines. For all work, uptake measured by T2 relaxation times. Error bars represent standard errors (n = 3).

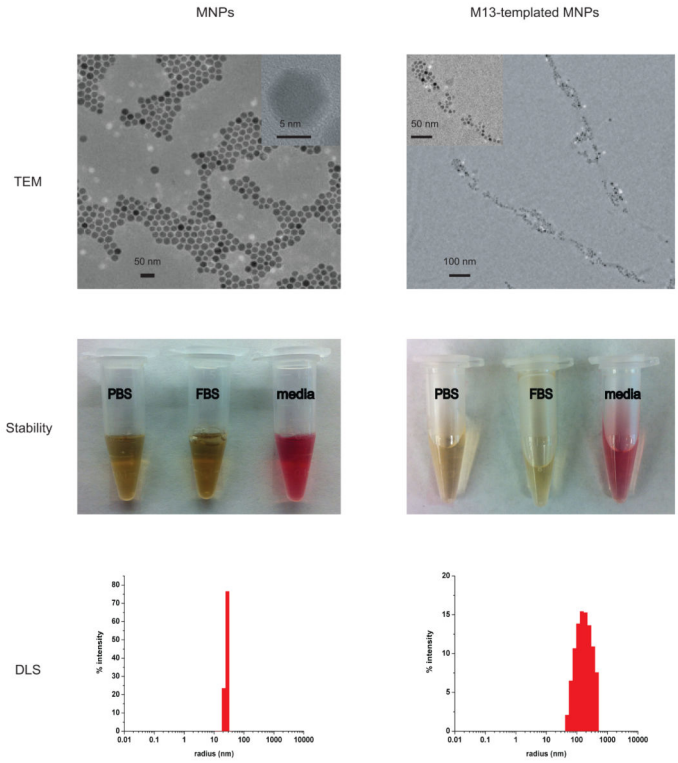

Figure 2. Material characterization of MNPs and M13-templated MNPs

TEM (top row), stability (middle row), and dynamic light scattering (DLS) (bottom row) of synthesized and assembled iron oxide nanoparticles along the p8 major coat of M13 (left and right column, respectively). TEM of MNPs and M13-templated MNPs with higher resolution images in inset. For stability, samples were resuspended in PBS (left), serum (fetal bovine serum (FBS), middle) and tissue culture media (right). For DLS, MNPs were water-solubilized with NH_2-PEG-DSPE (2000) and samples were run on a DynaPro Titan Light Scattering instrument at 10% power. Samples were run with n = 10.

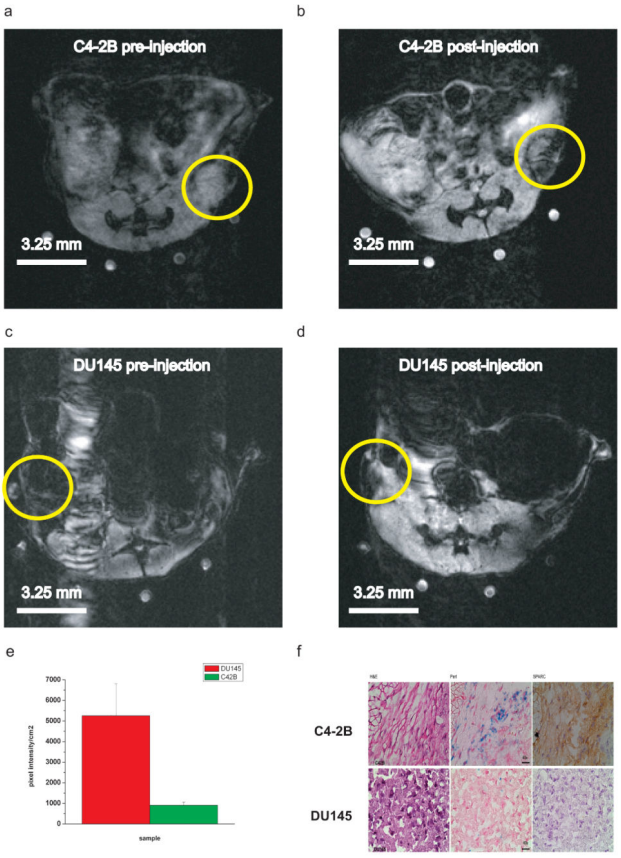

Figure 3. Targeting *in vivo* using MRI and correlative histology

a,**b,** MR scans of mice with C4-2B tumours (encircled) pre-injection and 24 h post-injection, respectively, with M13-SBP MNP. **c**,**d,** MR scans of DU145 control tumours (circled) pre-injection and 24 h post-injection with probe, respectively. Note the maintenance of the bright image of the tumour (circled) in DU145 pre- to post-injection, whereas a post-injection dark contrast against the pre-injection bright MR image is observed in C4-2B (circled). All tumours formed subcutaneously in athymic nude mice and imaged using 7 T small animal MR scanner. **e**, Tumour images were quantified for pixel intensities. Equivalent regions of interest (ROI) were marked around all tumours ~ 5 mm in diameter, and pixel intensity of the image was quantified using OsiriX imaging software and normalized to the area of the ROI. All images of tumours had similar areas and were taken from the same imaging depth from all mice (n = 5 for each group) to enable accurate comparison. Error bars represent standard error (n = 5). **f**, Histology for M13-SBP-MNP tumour accumulation. Tumours were sectioned and stained with H&E and Perl's reagent for the presence of iron. Tumour sections were also stained for SPARC expression using an anti-human SPARC antibody. Sections in blue suggest areas of iron oxide nanoparticle localization. Blue staining is present around the stroma in C4-2B sections (top row, middle column). There is no blue present in the DU145 control (bottom row, middle column). There is co-localization of SPARC expression (top row, far right) with iron accumulation in C4-2B tumours; there is no SPARC expression in DU145 tumours (bottom row, far right). All panels are at the same scale.

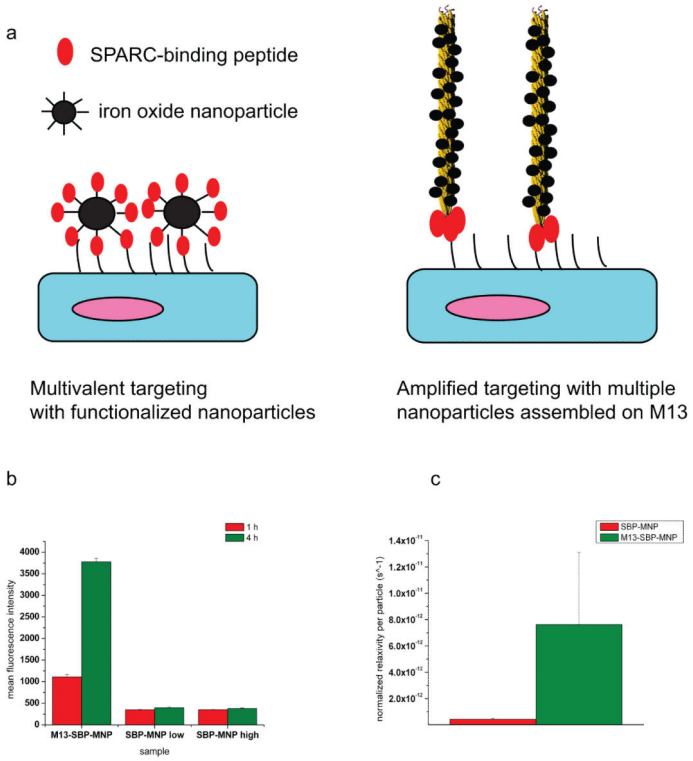

Figure 4. Amplified targeting *in vitro*

a, Left: schematic of SPARC-binding peptide ligand targeting of nanoparticles to targets via multivalent interactions. Right: M13 assembles multiple nanoparticles along its coat to deliver a higher cargo of nanoparticles per SPARC target than the ligand functionalized nanoparticles (left). **b**, C4-2B uptake of M13-SBP-MNP or functionalized MNPs with two different SBP concentrations as measured by fluorescence, at 1 h and 4 h respectively. **c,** Comparison of targeting of C42B using M13-SBP-MNP compared with peptide-functionalized MNPs (SBP-MNP), as measured by transverse relaxation. All error bars represent standard errors (n = 3).

Table 1

Relaxivities of various MR contrast agents at 0.47T, 40°C

Contrast agent	Relaxivity (R2) $[mMs]^{-1}$
Monocrystalline iron oxide nanoparticle (MION-46)	−34.8[19]
Cross-linked iron oxide (CLIO)	48[31]
Ferumoxtran	35.3[20,32]
Ferumoxide-Feridex	107[22]
Iron oxide nanoparticles (MNPs)	65.1
M13-templated MNPs	58.7